JOINT EUROPEAN TORUS JET

JET–P(84)05

Many Authors

JET Papers Presented at International Atomic Energy Agency

10th International Conference on Plasma Physics and Controlled Nuclear Research

12th–19th September, London, UK

JET Papers Presented at International Atomic Energy Agency

10th International Conference on Plasma Physics and Controlled Nuclear Research

12th–19th September, London, UK

Many Authors

JET-Joint Undertaking, Culham Science Centre, OX14 3DB, Abingdon, UK

CONTENTS

FIRST EXPERIMENTS IN JET

P H Rebut, D V Bartlett, G Bäumel, K Behringer, R Behrisch*, E Bertolini, C Best, R J Bickerton, F Bombi, J L Bonnerue, A Boschi, G BraccoV, M L Browne, M Brusati, A Bulliard, D J Campbell, P G CarolanΦ, J Christiansen, P Chuilon, J G Cordey, S Corti, A E Costley, G Decker**, K J Dietz, D F Düchs, G Duesing, R K F Emery, W W Engelhardt, T Eriksson, J Fessey, M J ForrestΦ, C Froger, K Fullard, M GadebergΔ, A Gibson, R Gill, A Gondhalekar, C Gowers, B J Green, G Grossot, N C HawkesΦ, J Hemmerich, M Huart, A Hubbard ††, C A Hugenholtz+, M Huguet, O N Jarvis, B E Jensen, E M Jones, G E Källne, J C Källne, H Krause*, P Kupschus, J R Last, E Lazzaro, P Lomas, G M McCrackenΦ, G Magyar, F K Mast*, M Mead, P L Mondino, P Morgan, A W MorrisΦ, L Nickesson, H Niedermeyer*, P Nielsen, P Noll, J Paillère, N J PeacockΦ, M Pick, J P Poffé, R Prentice, C Raymond, D C RobinsonΦ, R Ross, G Sadler, J Saffert, V Schmidt, F C Schüller, K Sonnenberg, M F Stamp, C A Steed, A Stella, P E Stott, D Summers, A Tanga, P R Thomas, G Tonetti°, E Usselmann, P van Belle, H van der Beken, J E van Montfoort, M L Watkins, J A Wesson, T Winkel, V ZanzaV, J Zwart.

JET JOINT UNDERTAKING, Abingdon, Oxon OX14 3EA, UK

+ EURATOM-FOM Association, FOM Instituut voor Plasmafysica, NL-3430 AA, Nieuwegein, The Netherlands

* EURATOM-IPP Association, IPP Garching, Federal Republic of Germany

Φ EURATOM-UKAEA Association, Culham Laboratory, Abingdon, Oxon OX14 3DB, UK

Δ EURATOM-RISØ Association, Risø National Laboratory, DK-4000 Roskilde, Denmark

V EURATOM-ENEA Association, Centro di Frascati, Casella Postale 65, 00044 Frascati, Italy

† EURATOM-CNR Association, Istituto di Fisica del Plasma, Via Bassini, 15, 20133 Milan, Italy

° EURATOM-Suisse Association, CRPP, CH-1007, Lausanne, Switzerland

** University of Düsseldorf, Düsseldorf, Federal Republic of Germany

†† Imperial College of Science and Technology, University of London, London, UK

FIRST EXPERIMENTS IN JET

ABSTRACT

The paper describes results obtained from JET since June 1983, which show that this large tokamak behaves in a similar manner to smaller tokamaks, but with correspondingly improved plasma parameters. Long duration hydrogen and deuterium plasmas (>10s) have been obtained with electron temperatures reaching >4keV, for power dissipations <3MW, and with confinement times up to 0.6s. Elongated plasmas (b/a in the range 1.1 - 1.7) have been achieved with plasma currents, I_p, up to 3.7MA and toroidal magnetic fields, B_T, up to 3.5T. At the highest elongations ($b/a \gtrsim 1.6$), loss of vertical stability occurred, as expected from previous calculations. Forces of several hundred tonnes (at I_p = 2.7MA) were transmitted to the vacuum vessel.

Measured confinement times are larger than the corresponding INTOR values. The maximum achievable density is limited by disruptions. Impurity levels determine this limiting density, and the paper concludes with proposals to reduce these. In addition, progress in neutral injection and RF heating is described, as well as preparations for D-T operation.

1. INTRODUCTION

The Joint European Torus (JET) (see Table I), which is the largest tokamak in operation, is the central project within the fusion programme of the European Community. As planned, first plasma operation was achieved on June 25, 1983, after a five-year construction period. This paper presents results from operation of Ohmically heated plasmas (volumes up to $130m^3$) with currents up to 3.7MA. Figs.1 and 2 show plan and meridional cross-sectional views of the JET torus.

2. MACHINE OPERATION

JET is pumped by 4 turbomolecular pumps (effective H_2 pumping speed 8500 $1s^{-1}$). Choice of suitable vessel materials (Inconel 600) and surface treatment (electropolishing), together with stringent quality procedures, resulted in a high quality vacuum.

Wall conditioning in JET uses RF assisted glow discharge cleaning in hydrogen at 2-5 x 10^{-3}mbar with a vessel temperature of 100-300°C. Typical cleaning after opening the vessel consists of a water rinse of the walls, pumping down, baking to 300°C for 48 hrs and glow discharge cleaning for 72 hrs. During discharge cleaning the impurity partial pressures increase by several orders of magnitude and the impurities are progressively removed. For tokamak operation at 250°C, UHV conditions obtained were 10^{-7}mbar total pressure, 10^{-7}mbar H_2 partial pressure and 10^{-9}mbar residual impurities, primarily CH_4, H_2O and CO. Pulse discharge cleaning has also been used, but no significant improvement in subsequent plasma performance was achieved.

Two gas introduction units were installed, each allowing fast puffing for prefilling, and for controlled addition of gas during the current pulse. These valves are fully metallic and bakeable to 300°C.

Four graphite limiters (40cm wide and 80cm high), fixed at the mid-plane and 212 mm protruding from the wall, are used to define the outer plasma boundary (See Fig.1). The limiters are curved in the toroidal direction to accommodate plasmas of different scrape-off layers (1-3cm thick). Two limiters are

As an additional safety measure, the vacuum vessel mounting will be strengthened.

4. DIAGNOSTICS IN USE

The following diagnostic techniques have been used. Their layout on the machine is indicated in Figs. 1 and 2:

a) Magnetics: Each octant of JET has been equipped with an identical set of poloidal field pick-up coils and differential flux loops. In addition, there are voltage loops and special flux loops, for plasma position control, and a diamagnetic loop. Signals from individual sensors are recorded with correcting information to form a basic data set for software processing. This data is processed to determine the magnetic structure of the plasma, including the effects of all poloidal field coils, the iron core and limbs with variable permeability, and the vacuum vessel (See Fig.2);

b) 2 mm Interferometer: This is a single channel 2 mm interferometer which gives the line averaged electron density, $\bar{n}_e$, along a vertical chord at R = 3.14m;

c) Reflectometry: A simple reflectometer has been used at a frequency fixed during a pulse, in the range 29 - 38 GHz. An O-mode wave is launched at the plasma in the midplane of JET along the plasma density gradient. The wave is reflected at the cut-off layer, whose spatial location is determined interferometrically. With increasing plasma density, the cut-off layer moves to larger values of R. By measuring the position of the cut-off layer as a function of time, and assuming that the profile shape remains unchanged while the local density changes, $n_e(R)$ has been determined (Fig.5(a));

d) ECE: Electron cyclotron radiation (2nd harmonic E-mode, 70 - 160GHz), emitted on one horizontal chord along the major radius 13cm below the mid-plane, is analyzed utilizing a scanning Michelson interferometer of period 15ms. The instrument is calibrated absolutely in the band 60 - 300GHz and shows absolute uncertainty of ±20% and relative uncertainty in profile shape of ±10%. The system provides spatially and temporally resolved (ΔR, $\Delta Z \sim$ 15cm, Δt = 15ms) electron temperatures. Harmonic overlap limits the region of temperature determination to 2.8m $<R<$4.2m, which allows measurement of about half the profile (Fig.5(b)). The measurements yield $T_e(|B|)$, and from calculations of $|B(R)|$, the profile $T_e(R)$ is deduced. Several hundred profiles are measured during a normal 10s JET pulse;

e) Bolometry: Space and time resolved measurements of radiation emissivity profiles are obtained with three arrays of collimated bolometers (3 fans containing a total of 34 detectors) viewing the plasma in orthogonal directions through vertical and horizontal ports in the same poloidal plane. In addition, 8 individual bolometers, one at each octant, are used to monitor toroidal symmetry of emission. A detection limit of 70μW/cm^2 at a time resolution of 20ms has been measured. With a 4μm thick gold absorber, the detector is sensitive in the wavelength range 0.15 - 200nm. From the measured intensities, radial profiles of local radiated power can be derived by Abel inversion, assuming elliptic flux surfaces;

f) Spectroscopy: During the year of operation, the range of wavelengths covered has been progressively increased. Initially, visible radiation (transmitted through $\sim$ 100m of optical fibres) was examined, yielding information on H_α emission, bremsstrahlung and the influx of light impurities. Currently, there are two

where η_o is the Spitzer resistivity for a pure plasma. This does not take account of trapped particle effects, which will reduce the Z_{eff} values by a factor of about 1.5. Z_{eff} increases with plasma current and decreases with density (Fig.7(a)).

The energy confinement time is defined as

$$\tau_\varepsilon = \frac{3}{2} \int (n_e T_e + n_i T_i)\, dV / P_\Omega$$

where P_Ω is the total ohmic input power. The ion deficiency factor is $n_i/n_e = (Z_i + 1 - Z_{eff})/Z_i$, where Z_i is the charge of the principal impurity. In all calculations, the density profile was that measured by the microwave reflectometer (Fig.5(a)), and the average ion temperature was taken as $0.9\bar{T}_e$.

In deuterium, a total energy confinement time of 0.6s has been achieved at $B_T = 3.4T$ and $\bar{n} = 3 \times 10^{19} m^{-3}$. The energy confinement time increases with density, which is limited by major disruptions, characterised by a sudden drop in temperature and a flattening of the current density profile. The operating range for flat-top electron densities and current densities is shown in Fig. 7(b). The maximum achievable density during the flat-top is shown as curve (i), and the critical density limit, $\bar{n}_c$, for disruptions, which usually occur during the current fall is indicated as curve (ii) [1]. Observations suggest that $\bar{n}_c$ can be increased with reduced impurity levels.

The current decay time during a disruption varies over a wide range depending on the ability of the equilibrium field system to respond to the change of equilibrium. In the case of elongated plasmas, current rearrangement leads to a more elliptic plasma which is vertically unstable. Operation with currents in excess of 3MA with high elongations has been avoided in order to limit the consequences of the vertical disruption. Therefore, the full potential of elongated plasmas has not been examined. For the limited data available, there are indications of improved energy confinement in elongated plasmas when density, current, and toroidal field are kept constant. However, the maximum confinement times are about the same in the two cases, since the critical density is lower for the same current in elongated plasmas.

The influence of the limiter safety factor, q_1, on the plasma behaviour has been examined. As q_1 is lowered, mhd signals (mainly m = 2, n = 1) increase in amplitude. The signal level is an order of magnitude larger for a discharge with $q_1 = 3.3$ (at 1.59T and 2.2MA) compared to an equivalent but larger discharge with $q_1 = 3.9$. However, the energy confinement time is not significantly reduced until the lowest value of q_1 (= 2.75) is reached.

Bolometric measurements show that at least 70% of the input power is radiated. In the central plasma region, less than 30% of the local input power is radiated (Fig.9). With the high central temperatures achieved, a medium Z material (such as Ni) would be needed to radiate in this region. The principal impurity elements observed in JET plasmas are carbon, oxygen, chlorine, chromium, nickel and molybdenum. Spectroscopic measurements indicate that a significant influx of impurities come from the limiter. Some (such as Mo) are known to have been deposited on the graphite limiter during manufacture; other impurities (such as Ni and Cr) come from the Inconel vessel walls during discharge cleaning, disruptions, and charge exchange sputtering.

walls easily and has low hydrogen retention characteristics. In addition, low radiative losses are expected. In order to limit thermal fluxes to the limiters, it might be necessary to control the edge temperature by neon puffing.

In the near future, extra protection using carbon tiles will be tested. Following the introduction of additional heating on JET, two toroidal belt limiters (toroidal rings situated 1m above and below the equatorial mid-plane) made of plates of either carbon or beryllium inserted between cooled fins will be installed in the machine in 1986.

7.2 Additional Heating

25 MW of additional heating will eventually be applied to JET: two Neutral Injectors will provide 10 MW and RF Heating at the Ion Cyclotron Resonance Frequency (ICRF) will provide a further 15 MW in the plasma (30MW from the generators) from 10 antennae disposed around the torus.

The first neutral beam injector designed to deliver 5 MW of 80 keV neutral hydrogen particles into the plasma will be installed in late 1984. The injector contains 8 ion sources, and ion beam pulses of 80 keV and 60A have been produced according to specification. Beam heated plasmas should be produced in 1985. Manufacture of all components for the second injector are well advanced and this should be installed later in 1985. It is planned to change to deuterium later, and a prototype source has already produced a beam of 160 keV deuterons to the required specification.

The ICRF heating system, together with the first two experimental antennae (without active cooling) will be installed in late 1984, for test purposes. There are several modes of heating, working either at the fundamental frequency of a minority species (e.g. ^{3}He in H and D in H), or at harmonics of the main ion species. The system's frequency range 25 to 55 MHz covers the different modes for the plasma species considered (D, H, T, ^{4}He and ^{3}He). By 1987, the two experimental antennae will be replaced by six actively cooled models providing 9 MW of heating in the plasma. Detailed preparation of special limiters and protection plates for these antennae, covered in low-Z material, are well advanced. Later, a total of ten antennae, providing 15 MW, should be available.

7.3 Preparation for Tritium Operation

During 1989-90, facilities for the study of α-particle heating in D-T plasmas should be available. Basic decisions concerning the on-site hydrogen isotope separation plant have been made. The plant will be based on gas chromatography and will allow recirculation of tritium into the vessel. The transfer pumps will be of the cryogenic type and the whole system, at present under detailed design, is conceived as a compact sealed unit requiring little maintenance during the final two years, for which tritium operation is foreseen. 2500 Ci of tritium will be introduced for each pulse and 10^{4} tritium pulses are planned. Remote handling facilities are also in preparation for progressive use as machine activation increases, first due to deuterium operation and later in D-T experiments.

REFERENCES

[1] WESSON J A, THOMAS P R et al; Plasma Physics and Controlled Fusion Research (Proc. 10th. Int.Conf., London, 1984);

[2] BEHRINGER K , TARONI A et al; Plasma Physics and Controlled Fusion Research (Proc. 10th. Int.Conf., London, 1984);

[3] CORDEY J G et al; Plasma Physics and Controlled Fusion Research (Proc. 10th. Int.Conf., London, 1984)

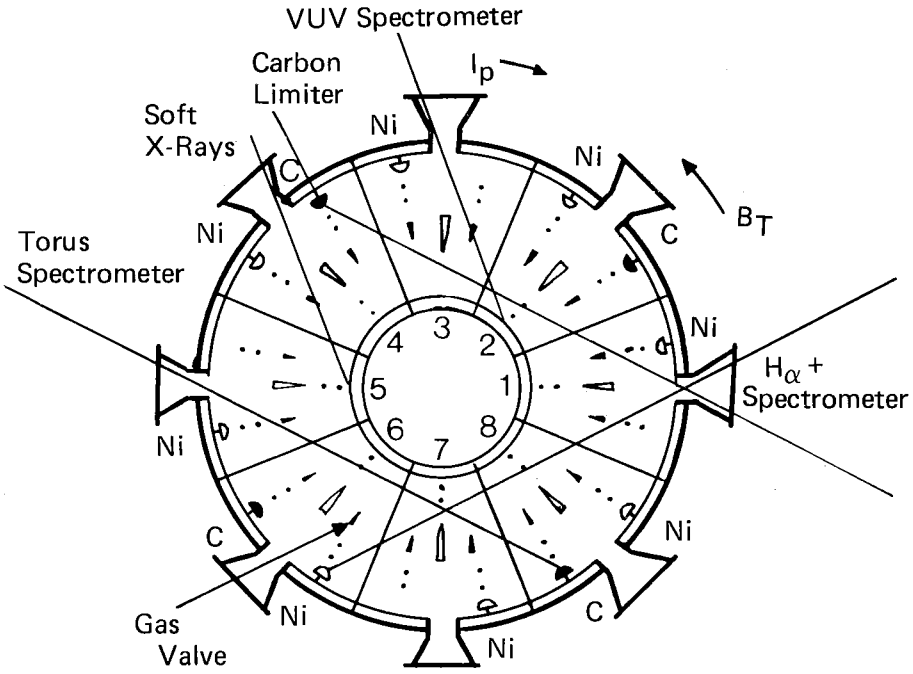

Fig.1: Toroidal cross-section of torus showing location of diagnostics, etc;

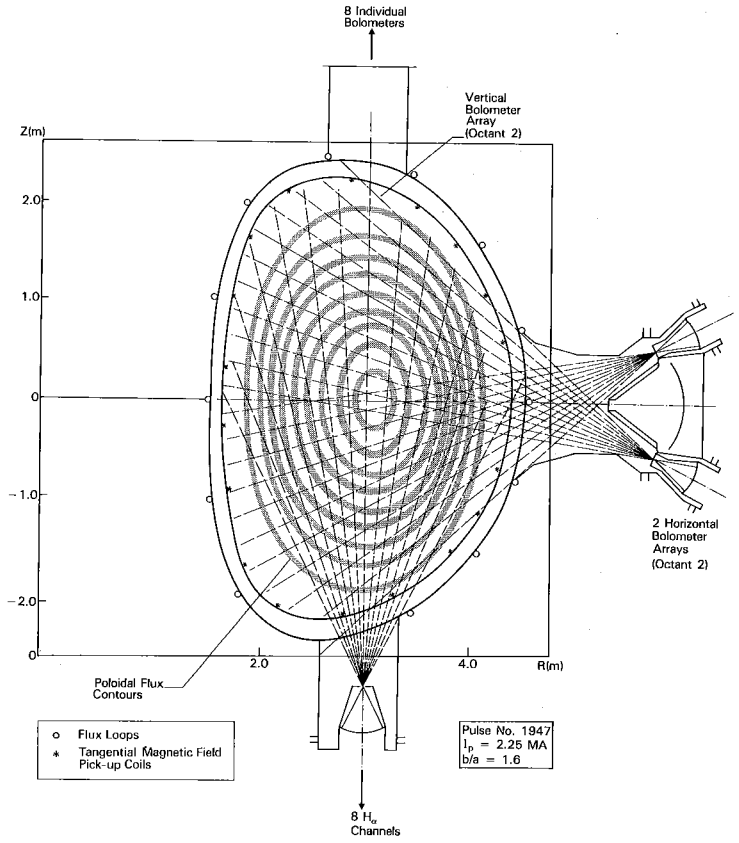

Fig.2: Poloidal cross-section of torus showing magnetic flux surfaces and area covered by radiation detecting diagnostics;

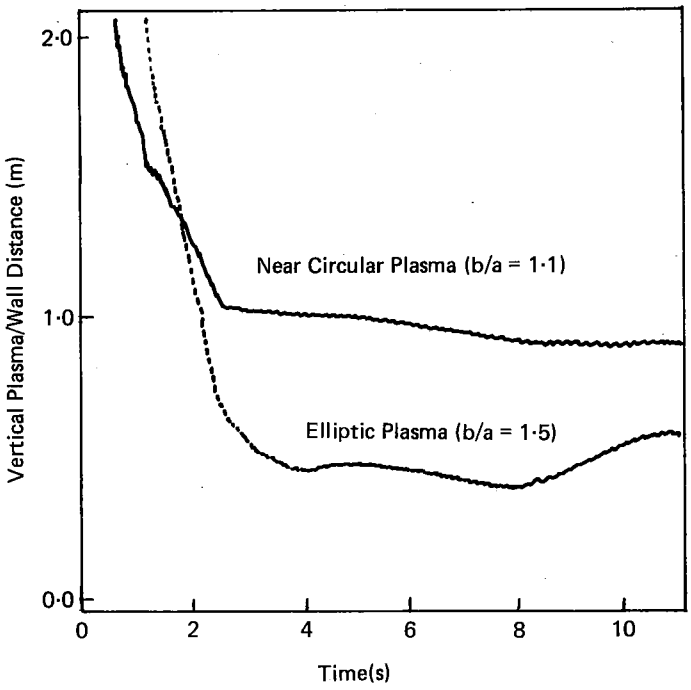

Fig.4: Vertical positioning - plasma-wall vertical distances versus time for b/a ∿ 1.1 and b/a ∿ 1.5;

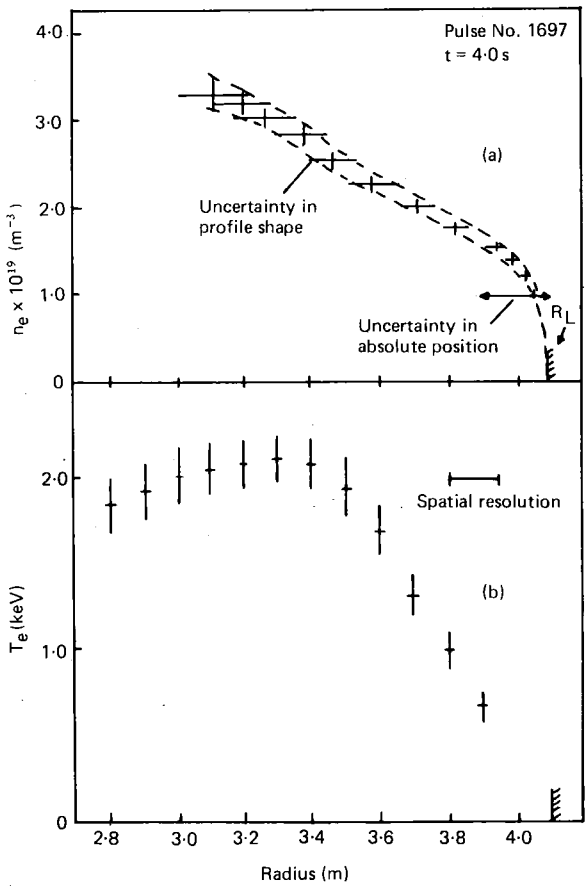

Fig.5: Typical profiles of (a) electron density (from reflectometer) and (b) electron temperature (from ECE);

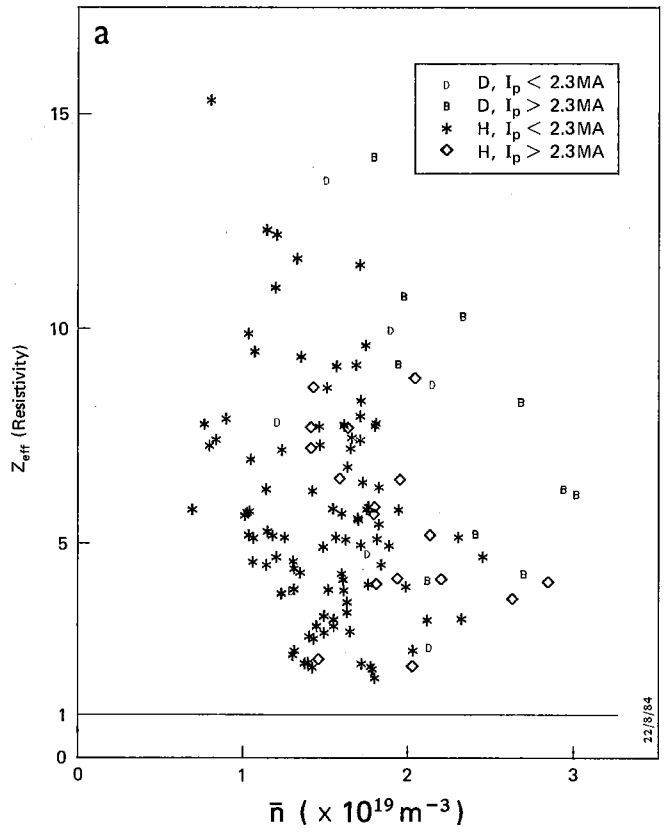

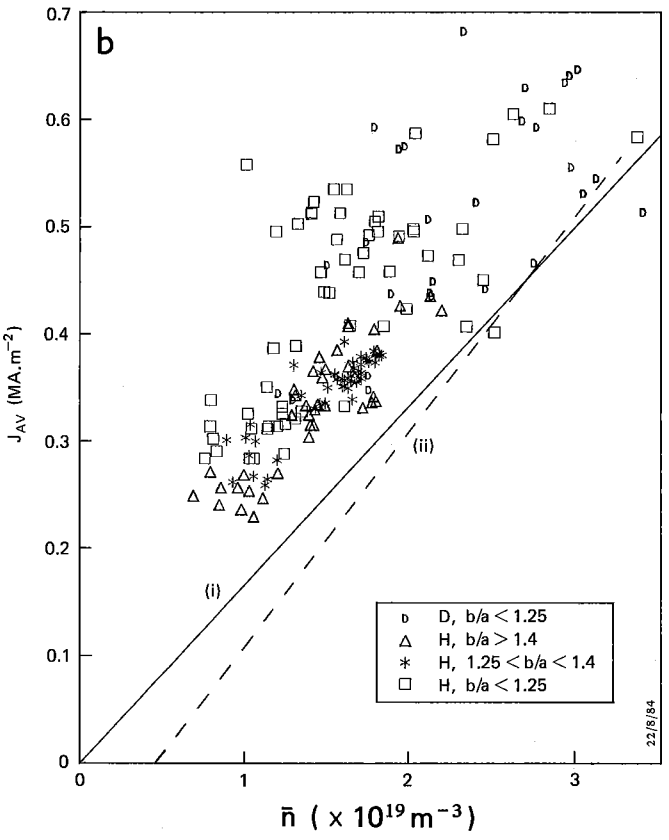

Fig.8: a) Z_{eff} versus n from resistivity;
b) Disruption boundary, plasma current density versus $\bar{n}$; [Curve (i) corresponds to $\bar{n}_c = 6 \times 10^{19} J_{av}(m^{-3})$ and curve (ii) is the disruption limit $\bar{n}_c = (0.45+5J_{av}) \times 10^{19} (m^{-3})$]

PARTICLE AND ENERGY CONFINEMENT IN OHMICALLY HEATED JET PLASMAS

J G Cordey, D V Bartlett, R J Bickerton, G Bracco[#], M Brusati, D J Campbell, J P Christiansen, S Corti, A E Costley, J Fessey, M Gadeberg[ϕ], A Gibson, R D Gill, N Gottardi, A Gondhalekar[+], C W Gowers, A Hubbard[x], C A Hugenholtz, O N Jarvis, L de Kock, H Krause*, E Lazzaro, P J Lomas, F K Mast*, P D Morgan, P Nielsen, P Noll, M Pick, R Prentice, R T Ross, G Sadler, F Schüller, M F Stamp, D Summers, A Tanga, P R Thomas, G Tonetti[°], P van Belle, V Zanza[#].

JET Joint Undertaking, Abingdon, Oxon, OX14 3EA, UK.

* EURATOM-IPP Association, IPP Garching, Federal Republic of Germany.
\+ EURATOM-FOM Association, FOM-Instituut voor Plasmafysica, NL.3430 AA, Nieuwegein, The Netherlands.
° EURATOM-Suisse Association, CRPP, CH-1007 Lausanne, Switzerland.
\# EURATOM-ENEA Association, Centro di Frascati, Casella Postale 65, 00044 Frascati, Italy.
x Imperial College of Science and Technology, University of London, London, UK.
ϕ EURATOM-RISØ Association, Risø National Laboratory, DK-4000 Roskilde, Denmark.

PARTICLE AND ENERGY CONFINEMENT IN OHMICALLY HEATED JET PLASMAS

ABSTRACT.

The particle and energy transport in Ohmically heated JET discharges has been analysed. The energy confinement time τ_E is found to increase with both plasma density, n, and safety factor q, with τ_E values in the range 0.1 to 0.6s. At low density, the particle confinement time, τ_p, increases with density, while for $\bar{n}_e \gtrsim 1.3 \times 10^{19} m^{-3}$ it decreases with density: the peak value is about 1s.

1. INTRODUCTION

A study was undertaken of the scaling of particle and energy confinement properties with the main plasma parameters, current, density etc., and compared with similar studies on smaller tokamaks [1] - [4]. Data obtained during the first year of operation was taken from about 200 discharges, about half had near-circular cross section and the other half were elliptical. In most of the plasmas the gas was hydrogen, towards the end of the year deuterium was used in near-circular cross section plasmas, and some 20 deuterium discharges are included in the data set. The paper is divided into three sections: plasma characteristics; energy confinement; and particle confinement.

2. PLASMA CHARACTERISTICS

Characteristic discharges had a long flat plateau (~4s) in both current and density, as shown in Fig.1. The data for scaling studies were extracted at the end of the flat top (indicated by * in Fig. 1(a)), so that transient effects could be ignored in the analyses. In all discharges, density and temperature sawtooth oscillations were present, indicating that the safety factor, q, in the plasma centre was less than unity.

The plasma geometry was varied from near-circular, with elongation K(=b/a)=1.15, to elliptical, with K = 1.6. The discharge flux surfaces at extremes of this range are shown in Fig.2, these were obtained by fitting the magnetic field from a Grad-Shafranov equilibrium solver [5] to the magnetic measurements made at the vacuum vessel wall. The minor radius, a, and major radius, R, were kept approximately constant at a = 1.1m and R=3.0m. The remainder of the parameters were varied in the ranges given below:-

$1.2MA < I < 3.5\ MA$ $\qquad$ $1.3T < B_\phi < 3.4\ T$

$2.6 < q_\psi(\text{Shafranov}) < 10$ $\qquad$ $1.7 < q_{cyl} < 6$

$0.7 \times 10^{19} m^{-3} < \bar{n}\ (\text{line average density}) < 3.4 \times 10^{19} m^{-3}$

The loop voltage on axis was between 0.6 - 1.2V: the lower values were found in the high B_ϕ discharges.

The radial electron temperature profiles were obtained from the electron cyclotron emission (ECE) at the second harmonic

average density is shown in Fig.5, together with INTOR scaling ($\tau_E = 4.5 \times 10^{-21}$ na^2). From the scatter, τ_E scaling with density alone is not sufficient. The separation of the data into bands depending on their value of q_{cyl} ($\cong 5a^2KB_\phi/RI$) shows that the safety factor is also an important scaling parameter. In fact, the main improvement in the energy confinement of the elliptic cross-section plasmas over the circular ones enters through the dependence of q_{cyl} on K. Using several combinations of I, n, B_ϕ, K and q_{cyl}, a regression analysis of the data set has been completed. The best combination found is $\tau_E = A\, n^\alpha q_{cyl}^\gamma$ with $\alpha = 1.15 \pm 0.15$ and $\gamma = 0.9 \pm 0.15$, the fit is shown in Fig.6. The deuterium points have been highlighted in Fig.6, showing the improvement in confinement of the deuterium discharges over those in hydrogen.

To obtain some indication of τ_E scaling with the plasma dimensions, the data has been compared with empirical scaling laws obtained from smaller tokamaks. Unfortunately there are a large number of these scaling laws. However, there are only three with a q dependence: (i) the DIII scaling law (which was obtained from a study of Ohmic heating experiments on DIII in circular [1] and non-circular [2] plasmas)

$$\tau_{Ee} = A_1 na^2 q_{cyl}^{3/4} \quad ;$$

(ii) the T11 scaling law [3]

$$\tau_{Ee} = A_2 q_{cyl}^{7/6} (a/R)^{5/24} R^{17/6} n B_\phi^{-1/3}$$

(iii) a recent scaling law derived from data on TFTR and PLT [4]

$$\tau_E = A_3 naR^2 q_{cyl}^{0.8}.$$

Comparing these expressions with JET data, it is found that, the TFTR/PLT scaling law gives the smallest scatter in the data points and the coefficient A_3 in JET 7×10^{-22} is only 10% less than the quoted value. The JET values for the other two coefficients are $A_1 = 4.7\times10^{-21}$ (for deuterium) which is 25% greater than the quoted value and $A_2 = 2.2\times10^{-22}$ which is 20% less than the quoted value. Both of these are just within the experimental errors of the measurements. Thus it appears that expression (iii) the R^2a scaling gives the best fit to the JET data, to be absolutely certain about this conclusion, experiments at large R and small a are required.

This section has shown that the energy confinement in JET increases with density and safety factor q_{cyl}, and so far no limitation with density has been found. Confinement in deuterium is better than hydrogen and the $R^2a\, nq_{cyl}^{0.8}$ scaling law gives the best fit to the data.

4. PARTICLE CONFINEMENT

The global particle confinement time, τ_p, has been evaluated by solving the particle balance equation $dN_e/dt = -N_e/\tau_p + \Sigma I$, where N_e is the total number of electrons in the plasma and ΣI is the rate of production of new plasma particles.

5. REFERENCES

[1] Ejima, S. et al, Nucl. Fusion, 22 (1982) 1627

[2] Nagami, M. et al, Nucl. Fusion, 22 (1982) 409

[3] Leonov, V.M. et al, Plasma Physics and Controlled Nuclear Fusion IAEA, Vienna, 1981 Vol. 1 p393

[4] Hawryluk, R.J. Recent results from TFTR. Proceedings of Conference on Heating in Toroidal Geometry, Rome 1984

[5] Brusati, M. et al, MHD Workshop, Lausanne 1983

[6] Chung, C.S. and Hinton, F.L., Phys.Fluids, 25 (1982) 1493

[7] Hubbard, A.E. et al, 9th Int. Conf. on Infrared and Millimetre Waves. Takarazuka, Japan 1984. To be presented.

[8] Johnson, L. and Hinnov, E., J. Quant. Spectro. Radiat. Transfer, 13 (1973), 333.

[9] Marmar, E.S., J Nucl. Materials, 76 & 77, (1978), 59.

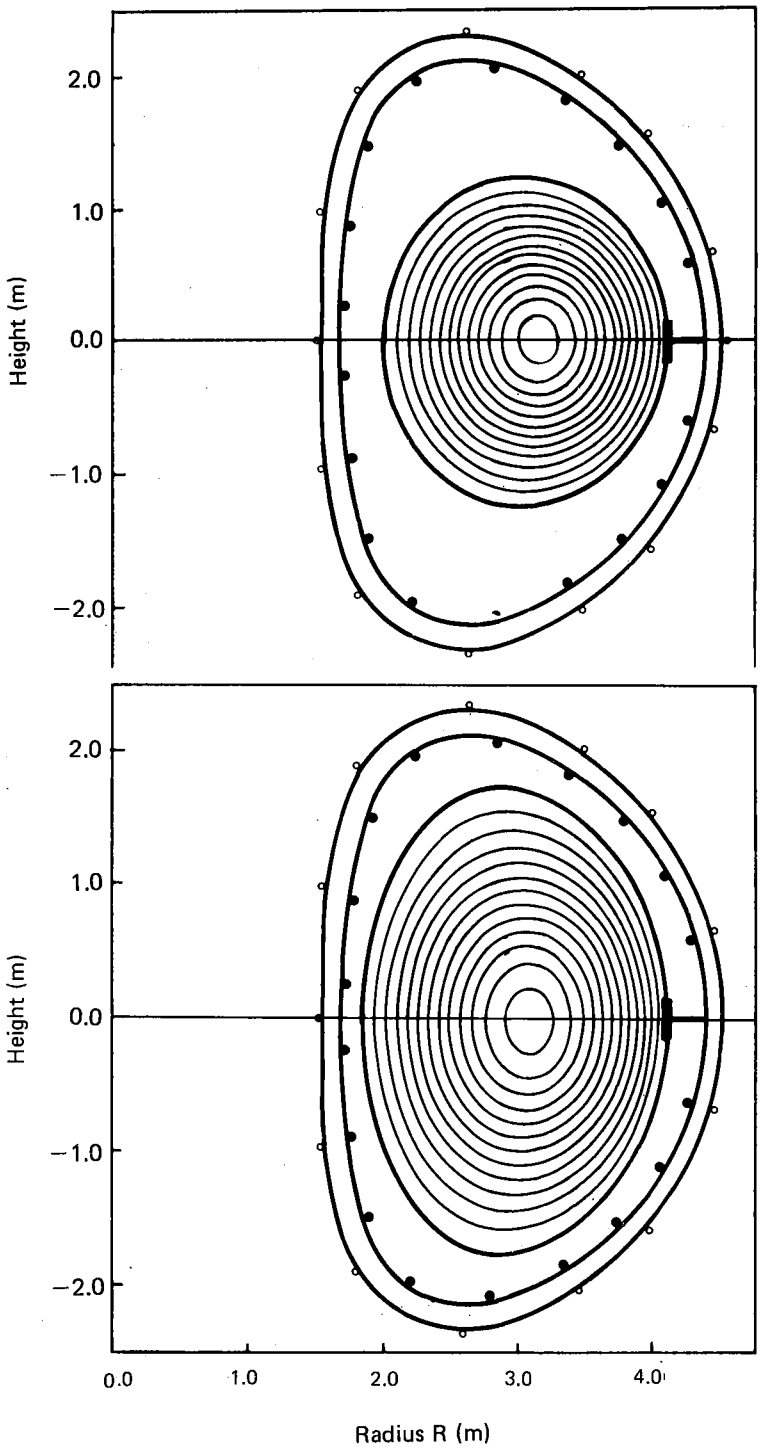

Fig.2 Cross-section through torus showing flux surface geometry, limiter and magnetic diagnostics for
(a) a near-circular discharge
I = 1.3MA, K(=b/a) = 1.16, β_p = 0.19 ± 0.1,
l_i = 1.23 ± 0.2, q_ψ = 4.2;
(b) an elliptical discharge
I = 2.8MA, K(=b/a) =1.54,
β_p = 0.12 ± 0.05, l_i = 1.1 ± 0.1, q_ψ = 3.6.

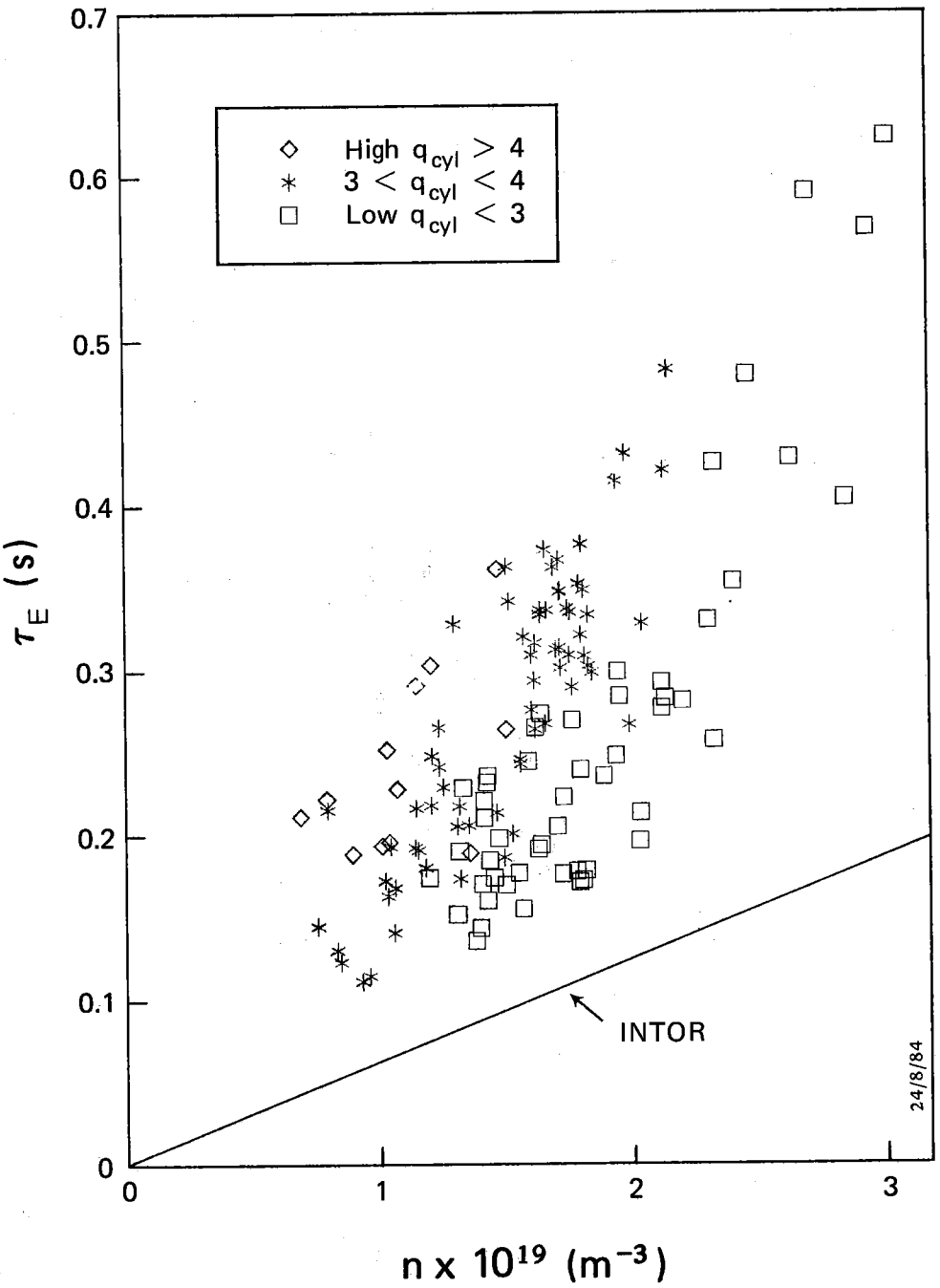

Fig.5 Total energy confinement time versus density for the data set, High $q_{cyl}>4$;. * $3<q_{cyl}<4$, low $q_{cyl}<3$; the line is INTOR scaling $\tau_E = 4.5 \times 10^{-21} na^2$. The dominant impurity is assumed to have $Z_i=12$.

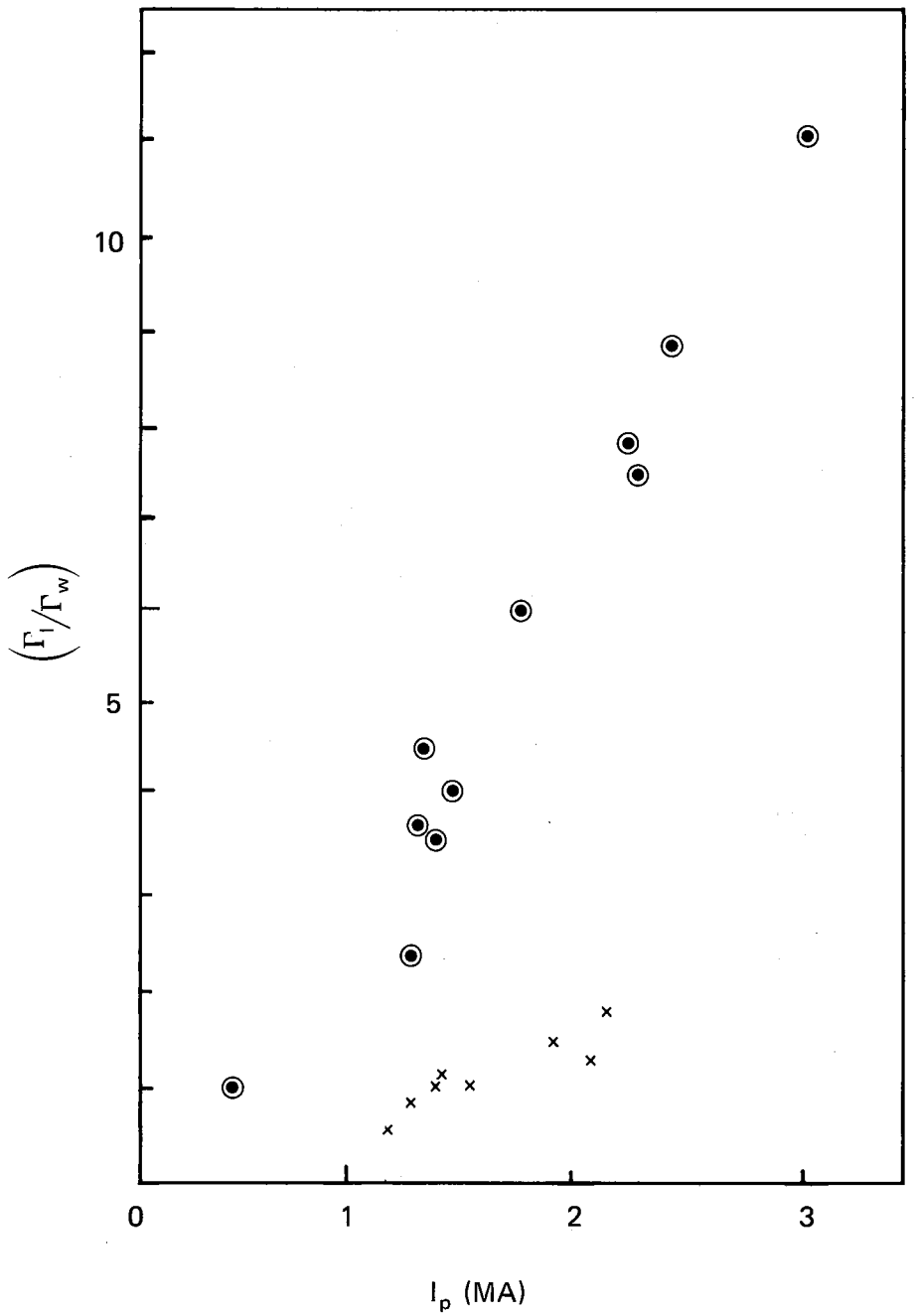

Fig.7 Ratio of limiter to wall fluxes of neutral hydrogen as a function of plasma current I(MA). Circles refer to plasma elongation of 1.2, and crosses to an elongation of 1.4.

IMPURITY STUDIES AND TRANSPORT CODE MODELLING OF JET PLASMAS

K H Behringer, A Abels-van Maanen†, J Bonnerue, A Bulliard, P G Carolan*, G Decker+, B Denne, D Düchs, J Ehrenberg+, W Engelhardt, M J Forrest*, R Gill, A Gondhalekar, N C Hawkes*, E Källne, H Krause, G Magyar, J L Martin, F Mast+, G M McCracken*, P Morgan, D Muir, J O'Rourke, N J Peacock*, A Ravestein, M F Stamp, P M Stubberfield, A Taroni, M L Watkins.

JET Joint Undertaking, Abingdon, Oxon OX14 3EA, UK

+ EURATOM-IPP Association, IPP-Garching, Federal Republic of Germany

† Mathematical Institute, University of Oxford, UK

* EURATOM-UKAEA Association, Culham Laboratory, Abingdon, Oxon, OX14 3DB, UK

IMPURITY STUDIES AND TRANSPORT CODE MODELLING OF JET PLASMAS

ABSTRACT

Impurities in JET are studied by visible and VUV spectroscopy, and from bolometer and soft X-ray signals. The measurements provide information on impurity influxes and densities in the plasma. These showed that light impurities could be controlled well initially, but subsequently were increasing. A relatively high level of metal impurities ($\sim$ 0.2%) is mainly responsible for high radiative power losses ($\sim$ 70%P_Ω). A wall material deposit on the graphite limiters is the primary cause of metal contamination. Molybdenum was present on the Carbon surfaces as a result of the manufacturing process. Chlorine is an abundant impurity, probably introduced when washing the torus.

Extensive transport code calculations have provided acceptably consistent models for present JET plasmas, taking account of transport, radiation and $q \lesssim 1$ activity. With the high levels of impurities present, it has been necessary to reduce the magnitude of several of the commonly used transport coefficients. In addition, the relation between the global confinement time and the assumed local transport coefficients was destroyed by both the $q \lesssim 1$ activity and impurity radiation. Control of metallic impurities should lead to improved performance.

1. DIAGNOSTICS FOR IMPURITY STUDIES

Spectroscopic instrumentation was limited to the visible and UV spectrum during July-December, 1983. Quartz fibres coupled the plasma light to filter boxes for H_α and continuum measurements. The H_α intensity was used for deriving the hydrogen particle confinement time and for recycling studies. The continuum at 523.5nm, checked for absence of line radiation, serves as a routine monitor of Z_{eff}. Optical fibres are simple and convenient in use and will operate during the active phase of JET, but restrict observation to wavelengths above 350nm. 8 vertical and 4 horizontal channels are installed: the latter view carbon or nickel limiters. These fibres also transmit light to three spectrometers, one equipped with a linear detector array (OMA); and the others provide photographic spectra or monitor selected impurity lines in the visible (OIV, CIII, NiXII). To extend the wavelength range into the UV, another spectrometer mounted close to the torus views a carbon limiter. It was used to study carbon and oxygen influxes, as well as metals (CrI, NiI, MoI) deposited on the carbon during operation. Recently, a VUV survey spectrometer (10-170 nm) was added, and the first spatial scan instrument is planned for late 1984.

Eight single bolometers mounted around the torus have checked toroidal symmetry (no significant asymmetries were

3. RESULTS

The first operation in June/July 1983 produced only low temperature (∿50eV), high loop voltage (∿14V), radiation - dominated discharges without sawtooth activity. Following more intensive cleaning since October 1983, JET has operated as a typical tokamak, with low loop voltage (∿1V), high central electron temperatures (1.5-3keV) and early sawtooth activity. However the impurity analysis has been complicated by the changing diagnostic capability, the varying state of cleanliness of the vacuum vessel and the differing modes of tokamak operation. In particular, the change from near-circular to elongated discharges has resulted in stronger interactions with the wall. The principal impurities are identified from the emission lines to be carbon, oxygen, chlorine, chromium, nickel and molybdenum. Chlorine is believed to come from the detergent used to wash the torus after a vacuum opening. Molybdenum was deposited on the limiter surface during the manufacturing process. The main flux of impurities comes from the surface of the limiter, as does the hydrogen. The impurity production rates at the limiter are approximately 2%, 10% and 2% of the hydrogen flux for metals, carbon and oxygen, respectively. From the intensities, the ratios of influx rates for the metals Ni:Cr:Mo are 7:1:1. The nickel and chromium are essentially wall material deposited on the limiters during glow discharge cleaning and disruptive discharges.

The bolometers show that typically 70-100% of the input power is radiated (Fig.2), almost independently of electron density and with approximately constant radiated power density in the plasma. With the known plasma temperatures, only the metals can be responsible for this radiation in the plasma bulk. Estimates of the metal content, taking as representative the coronal radiating effciency of nickel, yield values of 0.1-0.3%n_e ($n_e \sim 2\times10^{19}m^{-3}$). These were much the same during all the operating periods. Higher metal levels are found when light impurities are reduced and vice versa.

The chlorine, carbon and oxygen levels have been more variable. They reached a low point in October 1983 of 0.5% oxygen and carbon (Z_{eff}=3-4) to 2% oxygen and carbon, and 0.5% chlorine (obtained from the VUV survey instrument) in May 1984. This latter combination gives Z_{eff} ∿5.5 with about equal contributions from chlorine, nickel and oxygen.

Generally impurity levels increase with input power and decrease strongly with density. Fig.3 shows Z_{eff} as a function of n_e illustrating both the density dependence and the variation with the various campaigns on the machine. For the same conditions, Z_{eff} is consistently higher in 1984 than in 1983. The electron temperatures show the same trend maintaining a more or less constant loop voltage (0.8-1.2V) for the whole data set.

4. SIMULATING JET PLASMAS

Many expressions for anomalous electron thermal

end of the experimental error range is needed for acceptably low average temperatures and Ohmic input power (Table I). A higher nickel concentration (closer to that observed) can be tolerated with trapped particle corrections. Notice however, that the estimates of impurity concentrations are rather uncertain.

6. EFFECTS ON τ_E ASSOCIATED WITH $q \lesssim 1$ REGION AND IMPURITIES

With all models, the effects of $q \lesssim 1$ activity is to limit the central temperature, and to couple more strongly the central region with the edge, thereby decreasing τ_E and introducing a q dependence different from that found in χ_e (Fig.4).

Impurities can change the dependence of τ_E on size, as illustrated for χ_{eAI} in Fig.5. For a pure plasma, $\tau_E \sim \bar{a}^2$ but when impurity radiation is taken into account, $\tau_E \sim \bar{a}^{0.5}$. To recover the orginal scaling, it is necessary to modify substantially the impurity contant ($n_{Ni} \sim \bar{a}^{-4}$ is illustrated).

Computations of the time evolution of discharges indicate that reducing the light impurities, and hence Z_{eff}, without reducing the metal concentration, causes difficulties in overcoming radiation at low temperatures and in producing peaked current density profiles. On the other hand, reducing the metal concentration appears to be beneficial, even keeping the same level of light impurities. The radiated power can be reduced to about 20% of the Ohmic input and τ_E increases, by more than 50% in the case of χ_{eM}, χ_{eT11} and χ_{eNA}.

7. CONCLUSIONS AND FUTURE PLANS

Initially, JET appeared to control light impurities well, by baking and glow discharges. However, they have increasingly become a problem. Metallic impurities (Ni, Cr, and Mo) are mainly responsible for high radiation power losses (70-100% P_Ω). Fortunately, the local radiation on axis is much lower than the local Ohmic input (10-30%), so that energy confinement times would be derived with reasonable significance. Metal deposition on the carbon limiters is the main cause of metals in the plasma. Oxidation of these metals, when opening up the machine, may also be responsible for the oxygen increase. Chlorine is an abundant impurity, probably introduced by washing the torus.

Transport code simulations emphasise the effects of high levels of impurity concentrations. In particular, transport coefficients such as χ_{eAI}, χ_{eNA}, χ_{eT11} predict a lower τ_E (by more than 50%) than measured in present discharges, unless reduced values are used. Scaling laws of the global energy confinement time cannot easily be interpreted in terms of χ_e. Only very preliminary conclusions are possible on the functional dependence of χ_e and on the trapped particle correction in the resistivity.

TABLE I

	$\bar{n}_e$ ($\times 10^{19} m^{-3}$)	$\hat{T}_e$ (keV)	$\bar{T}_e$ (keV)	τ_E (s)	P_Ω (MW)	P_{RAD} (MW)	Z_{eff}
Experiment	1.8±10%	2.3±20%	.75±20%	.30±30%	2.2±10%	1.8±10%	5.5±30%
$\frac{\chi_{eAI}}{2.5} = \frac{2\times10^{19}}{n_e}$	1.8	1.9	.74	.29	2.1	1.7	5.3
$\frac{\chi_{eNA}}{1.7} = \frac{2.6\times10^{20}\varepsilon}{n_e R}$	1.7	2.6	.74	.30	2.0	1.8	5.5
$\frac{\chi_{eT11}}{3} = \frac{10^{21} T_e^{1/2} \varepsilon^{7/4}}{n_e q R}$	1.8	2.5	.77	.32	1.9	1.8	5.5
$\chi_{eCMG} = \frac{.284\times10^{16} B\varepsilon}{n_e^{0.8} q T_e}$	1.8	2.5	.70	.28	2.0	1.8	5.5
$\chi_{eM} = \frac{1.46\times10^{19} I^{0.8}}{n q T_e^{3/4}}$	1.8	2.4	.70	.29	2.0	1.6	5.5
$\frac{*\chi_{eAI}}{2} = \frac{2.5\times10^{19}}{n_e}$	1.8	2.4	.88	.30	2.5	1.9	4.2
$\frac{*\chi_{eNA}}{1.4} = \frac{3.1\times10^{20}\varepsilon}{n_e R}$	1.8	2.6	.82	.28	2.6	1.8	4.1
$\frac{*\chi_{eT11}}{3.3} = \frac{9\times10^{20} T_e^{1/2} \varepsilon^{7/4}}{n_e q R}$	1.8	2.6	.89	.31	2.5	2.3	4.5
$*\chi_{eCMG} = \frac{.284\times10^{16} B\varepsilon}{n_e^{0.8} q T_e}$	1.8	2.6	.83	.30	2.4	1.8	4.1
$*\chi_{eM} = \frac{1.46\times10^{19} I^{0.8}}{n q T_e^{3/4}}$	1.8	2.8	.89	.31	2.4	1.9	4.5

* With trapped particle corrections to resistivity.
Units are those used in the text, with ε the local inverse aspect ratio.

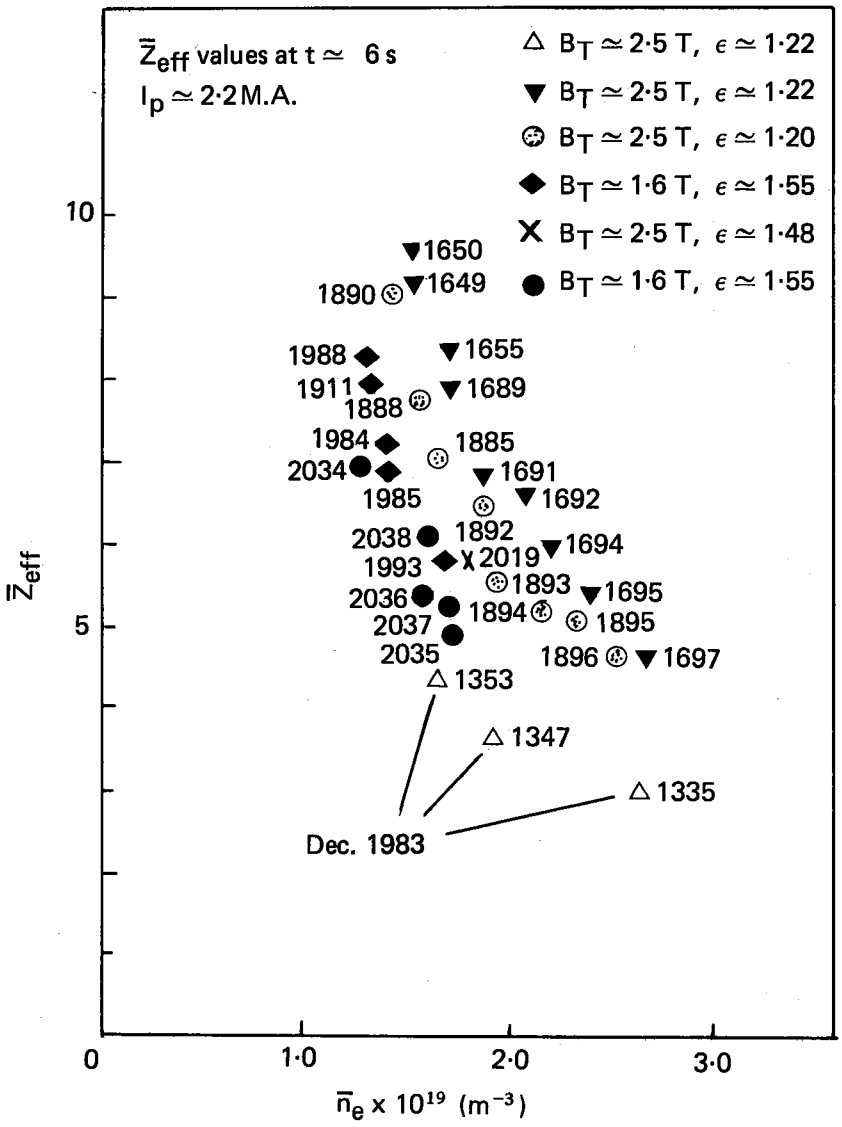

FIG. 3 Z_{eff} versus electron density for several experimental periods. (ϵ is the plasma elongation).

MHD BEHAVIOUR AND DISCHARGE OPTIMISATION IN JET

P R Thomas, J A Wesson, F Alladio[Δ], D Bartlett,
K Behringer, R J Bickerton, M Brusati, D J Campbell,
J P Christiansen, J G Cordey, A E Costley, F Crisanti[Λ],
K J Dietz, P A Duperrex[†], W Engelhardt, A Gibson, R D Gill,
N Gottardi, C W Gowers, B J Green, J L Hemmerich,
C A Hugenholz*, M Huguet, R Keller[†], L de Kock, H Krause[+],
J Last, E Lazzaro, F K Mast[+], P Morgan, A W Morris[∇],
H Niedermeyer[+], P Noll, M Pick, A Pochelon[†], P H Rebut,
D C Robinson[∇], R T Ross, G Sadler, F C Schüller,
T E Stringer, D Summers, A Tanga, G Tonetti[+], P van Belle.

JET Joint Undertaking, Abingdon, Oxon, OX14 3EA, UK

* EURATOM-FOM Association, FOM Instituut voor Plasmafysica, Postbus 7, NL-3430 AA, Nieuwegein, Netherlands.

\+ EURATOM-IPP Association, Max-Planck Institut für Plasmaphysik, D-8046 Garching bei München, Federal Republic of Germany

† EURATOM-Suisse Association, CRPP-CH 1007 Lausanne, Switzerland

∇ EURATOM-UKAEA Association, Culham Laboratory, Oxon OX14 3DB, UK

Δ EURATOM-ENEA Association, ENEA Centro di Frascati, C.P. 65-00044, Frascati, Italy

MHD BEHAVIOUR AND DISCHARGE OPTIMISATION IN JET

ABSTRACT

The electron density in JET is limited by disruptions, the disruption boundary having rather precise dependence on the plasma current. Disruptions on the current fall are preceded by a reduction in the rate of fall of electron density, this reduction being correlated with the spectroscopic signals. During the current quench which follows the disruption, the energy loss is predominately due to radiation from impurities, this radiation producing a cold, highly resistive plasma.

The observation in some discharges of m=2 magnetic fluctuations during start-up, while q_a is still above 10, indicates a rapid peaking of the current. Higher m-modes are found to be correlated with broad current-profiles. The growing magnetic oscillations which appear before disruptions often become phase locked but the amplitude of the non-oscillatory signal continues to grow. In some cases, the growth of the magnetic perturbation occurs entirely without oscillation.

Soft X-ray sawtooth oscillations are observed on all high current discharges, the period being typically 30-40ms. The onset is sometimes accompanied by oscillations at $\sim$500Hz. A comparison of the period of the oscillations with theoretical predictions has been made.

JET plasmas are vertically unstable, if b/a exceeds 1.2. The growth of the instability is limited by eddy currents induced in the vacuum vessel, allowing the plasma postion to be feedback stabilised. The loss of stabilisation in one discharge caused a force of hundreds of tonnes to be transmitted to the vacuum vessel.

1. INTRODUCTION

Since JET [1] became operational in June 1983, operating conditions for ohmically heated discharges have been established. JET is similar in size and plasma current to the proposed next generation of reactor-like tokamaks (e.g. NET), so the experience gained should have a substantial impact on their design. This paper describes some relevant experimental results.

2. START UP AND CURRENT RISE

Numerical studies were performed to define the optimum magnetic field configuration for start-up, taking into account the iron transformer circuit and eddy currents in the vacuum vessel. The resulting choice of coil turns, which minimise the dipole and quadrupole fields, permitted successful operation. Breakdown for pulse discharge cleaning was obtained at 7V per turn in a toroidal field of 0.15T, indicating that stray fields were very low. For tokamak operation, with 20V per turn at 2.6T, the filling pressure was in the range 2-4 x 10^{-5}mbar. Subsequent discharge behaviour showed strong dependence on filling pressure. The appearance of m=2 instabilities in many

4. MHD INSTABILITIES

Poloidal field coils, with a frequency response to 10kHz, inside the vessel and 14 external saddle loops on each octant have been used to investigate magnetic activity. The observed fluctuation frequency is independent of mode number and varies between 0.7 and 1.4kHz, for all elongation ratios. The apparent motion is in the electron diamagnetic drift direction (antiparallel to the plasma current.) The mode numbers, determined from the phase and amplitude variations of poloidal field signals, agree provided the vessel is assumed to have a conducting wall for rotating modes. Poloidal mode numbers m=5, 4, 3, 2 and toroidal mode number n=1 have been identified at fluctuation levels ranging up to 3% of the poloidal field at the resonant surface.

During the first second of the current rise, mode activity is complex, often displaying m=2 and 3 'soft' disruptions at early times, sometimes followed by m=4, when the current channel expands. Early m=2 activity develops in several ways: it can decay at constant frequency to an undetectable level; alternatively, it slows down and locks, followed either by a decay or a disruption. The plasma usually recovers from this unstable period. Occasionally, this phase of the discharge shows only low level m=4 activity, but later behaviour is not significantly different. The presence of high m (>4) modes is correlated with broad hollow current and temperature profiles. In the flat-top phase of some discharges, fluctuation levels fall to less than 0.01% of the poloidal field at the resonant surface and the corresponding island width to less than 1% of the plasma radius. For safety factors below 3 for circular, and 4 for elongated discharges, the m=2, n=1 activity increases rapidly, as shown in Fig.2a.

Fig.2b shows typical waveforms of a disruption. The final sawtooth is evident on the soft X-ray signal as the m=2, n=1 mode grows. The mode frequency falls from the usual 1kHz and, in this situation, the growth time is estimated to be 10ms. The mode then locks for 20-100ms. The growth is nearly linear when locked, with the perturbed field increasing by up to a factor of two. The final perturbation level is $\sim$3% at the resonant surface, which corresponds to an m=2, n=1 island width of 20% of the plasma radius. This does not extend to the limiter but approaches the q=3 surface. The internal inductance changes by less than 0.1% and the average density by less than 5% during mode growth and locking. The current termination starts with a fast mode whose growth time is less than 200μs and whose dominant component is m=2, n=1. In some cases, disruptions have no oscillatory magnetic precursor but multipolar analysis of the magnetic signals indicates a growing, but phase locked, m=2, n=1 mode.

5. SAWTEETH

Sawtooth oscillations are seen on the soft X-ray signals on all high current pulses. They usually start during the current rise, about 1-2s after breakdown. Soft

disruption or the behaviour of the thyristor bridge. In one discharge, a vertical instability occurred during the current-rise, when b/a was 1.7 and the current was 2.7MA. The plasma column moved down approximately 1.0m and the current decayed by 0.3MA in the first 50ms. In the next 30ms, the current decayed to zero. The plasma position estimation is uncertain for this phase due to of the eddy currents in the vacuum vessel which had a net toroidal component of 0.5MA. During this instability and termination, the vacuum vessel, which weighs 100t, was subjected to a considerable shock and underwent a complex, damped oscillation with a peak displacement of order .01m. Since the plasma inertia is negligible, the force balance must have been maintained throughout the instability and termination. A force imbalance of several hundred tonnes is calculated for maximum plasma displacement. A poloidal plasma current, which returns through the vacuum vessel, is suggested to explain this imbalance and the mechanical shock is due to the interaction of the vessel current with the toroidal field. The plasma motion across the magnetic field gives sufficient voltage to drive the current.

7. FLUX CONSUMPTION

The flux consumption, measured at the ohmic heating primary terminals and the flux loops on the vacuum vessel, agrees with calculations from a static equilibrium code and a constant resistive voltage drop of 0.8-1.2V. Current density profile changes were taken into account by constraining the safety factor on axis to 0.8, in the equilibrium code calculations. A satisfactory approximation is to represent the flux consumed at the any point by

$$\psi(t) = \{1.5 \pm 0.5 \;+\; M I_p \;+\; V_R t\} \quad (Wb)$$

start-up; inductive; resistive

Where M is a mutual inductance which represents the equilibrium flux distribution and whose value ranges from 2.2μH at the limiter to 4.3μH at the ohmic heating primary terminals. The flux consumed in establishing the plasma current distribution is included in the start-up term. The breakdown loss is 0.2 to 0.5Wb.

The flux available on the magnetic axis of a 5MA discharge is 54Wb at β_p=0 and 66Wb at β_p=1.5. 36Wb is obtained from the ohmic heating primary and the rest from the vertical field. The plasma inductance is approximately 8μH, and, consequently, 5MA discharges of duration of 10s or more can be made, provided the full magnetising current can be used without causing disruptions.

8. REFERENCES

1. Paper A-I-1 this conference
2. JAHNS G L, et al., Nucl.Fusion 18 (1978) 609
3. McGUIRE K, ROBINSON D C, Nucl.Fusion 19 (1979) 505
4. We are grateful to K McGuire for this information

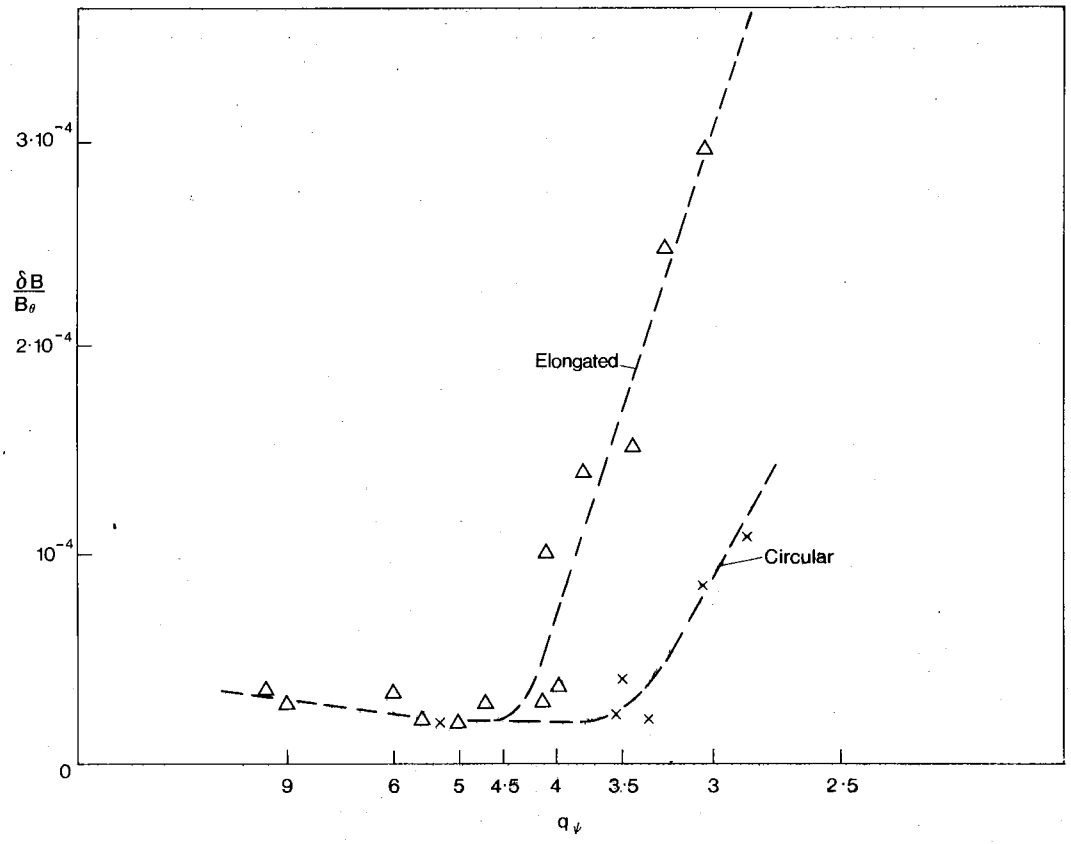

Fig.2(a) Magnetic fluctuation level as a function of the surface value of the safety factor.

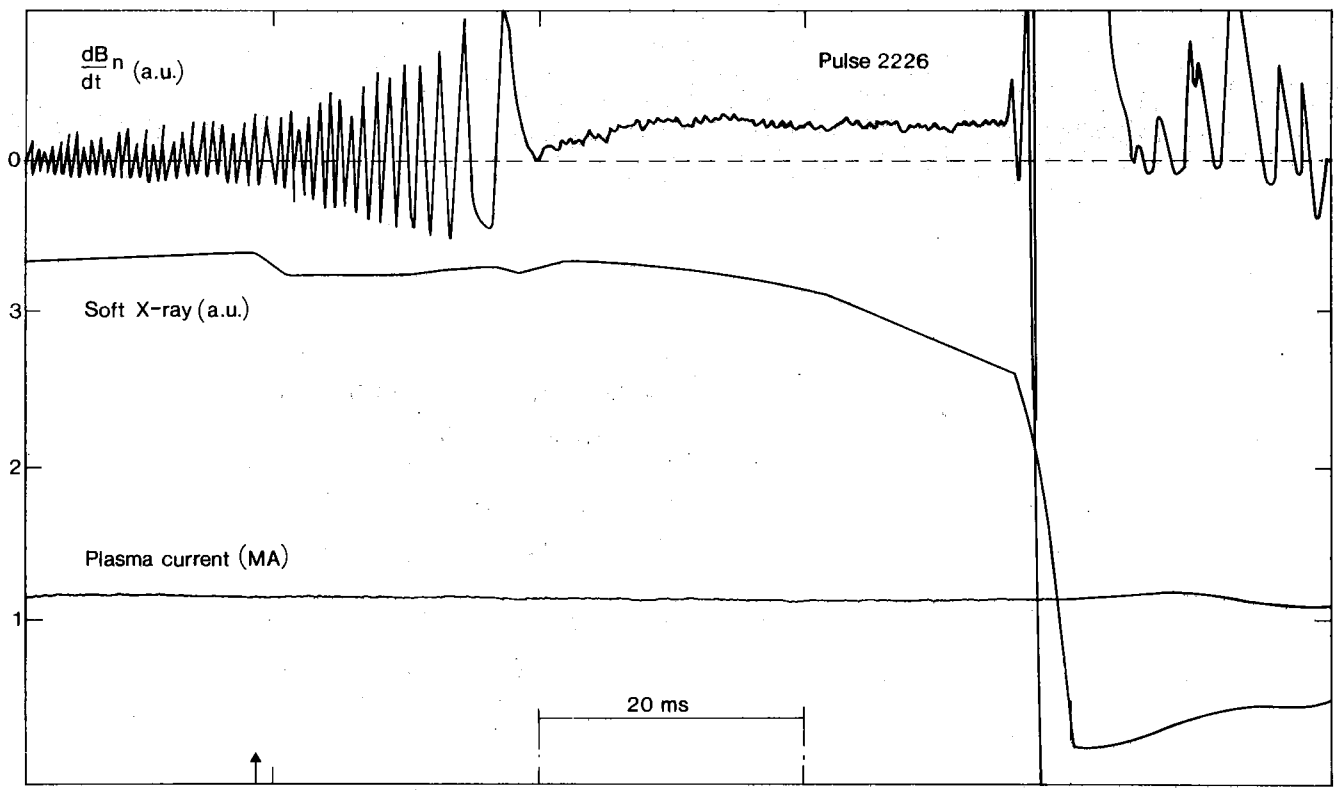

Fig.2(b) Waveforms at a disruption showing the magnetic fluctuations, the soft X-ray emission and the plasma current.

THERMAL INSTABILITY AND DISRUPTIONS IN A TOKAMAK

P.H. Rebut, M. Hugon

JET Joint Undertaking, Abingdon, Oxon. OX14 3EA

THERMAL INSTABILITY AND DISRUPTIONS IN A TOKAMAK

ABSTRACT

This paper develops a theoretical model, in which it is predicted that a major cause of anomalous confinement and disruptions in tokomaks is thermal instability. Due to the large thermal conductivity along magnetic field lines, the confinement is assumed to be poor in regions where the lines of force have an ergodic behaviour in contrast to the regions where the magnetic surfaces are nested (laminar case or islands). The ergodic region results from the interaction between chains of islands. It is shown that thermal islands can grow, when $\mathscr{P}_V/q'$ is negative, where $\mathscr{P}_V$ is the net power input to the electrons in the island (excluding thermal conduction) and q' is the radial gradient of the safety factor q. Conclusions are drawn on the occurrence of disruptions (critical electron density) and on confinement in the outer region of the plasma. Finally, suggestions are made to increase the critical density at which disruptions occur.

$$\begin{cases} \mathbf{B} = B_h\,\mathbf{e_h} + \nabla\mathscr{A} \times \mathbf{e_h} & (1) \\ \mathbf{J} = J_h\,\mathbf{e_h} + \nabla\mathscr{H} \times \mathbf{e_h} & (2) \end{cases}$$

with:

$$\mathbf{e_h} = \frac{p}{p^2+r^2}\,(r\,\mathbf{e}_\theta + p\,\mathbf{e}_z) \qquad (3)$$

Ampère's law in helical geometry is:

$$\begin{cases} \Delta_h\mathscr{A} = \dfrac{2p}{p^2+r^2}\,B_h - 4\pi\,J_h & (4) \\ B_h = 4\pi\,\mathscr{H} & (5) \end{cases}$$

with:

$$\Delta_h = \frac{p^2+r^2}{pr}\,\frac{\partial}{\partial r}\left(\frac{rp}{p^2+r^2}\,\frac{\partial}{\partial r}\right) + \frac{p^2+r^2}{p^2r^2}\,\frac{\partial^2}{\partial s^2} \qquad (6)$$

The plasma balance equation $\nabla P = \mathbf{J} \times \mathbf{B}$ is:

$$4\pi\,J_h = 4\pi\left(\frac{p^2+r^2}{p^2}\right)\frac{dP}{d\mathscr{A}} + \frac{1}{2}\,\frac{dB_h^2}{d\mathscr{A}} \qquad (7)$$

If the helical flux $\mathscr{A}$ is a function of r only: $\mathscr{A}=\mathscr{A}_o(r)$, Eq. (1) yields:

$$\nabla\mathscr{A}_o(r) = B_\theta\left(\frac{q}{q_o} - 1\right)\mathbf{e_r} \qquad (8)$$

with:

$$p = q_o R \quad \text{and} \quad q = \frac{r\,B_z}{R\,B_\theta} \qquad (9)$$

If q_o corresponds to the value of q at $r = r_o$, $q_o = q(r_o)$, the expression for $\mathscr{A}_o(r)$ in the vicinity of r_o is:

$$\mathscr{A}_o(r) = \frac{1}{2}\,B_\theta\,\frac{q'}{q_o}\,(r-r_o)^2 \qquad (10)$$

2.2 Perturbation theory - external solution.

In the regions where the plasma pressure is small, $\frac{dP}{d\mathscr{A}}$ can be neglected in Eq. (7). Let $\mathscr{A}(r,s)$ be:

$$\mathscr{A}(r,s) = \mathscr{A}_o(r) + \tilde{\tilde{\mathscr{A}}}(r,s) \qquad (11)$$

where $\mathscr{A}_o(r)$, defined by Eq. (10), is a solution of Eq. (4) and $\tilde{\tilde{\mathscr{A}}}(r,s) < \mathscr{A}_o(r)$.

$$\text{If} \quad \begin{cases} \delta B_h = B_h(\mathscr{A}(r,s)) - B_h(\mathscr{A}_o(r)) \ll B_h \\ \delta J_h = J_h(\mathscr{A}(r,s)) - J_h(\mathscr{A}_o(r)) \ll J_h \end{cases} \qquad (12)$$

and after combining Eqs. (4), (7) and (8), we find that $\tilde{\tilde{\mathscr{A}}}(r,s)$ is a solution of:

$$\mathscr{A} = \frac{1}{2}\frac{r_o}{R} B_z \frac{q'}{{q_o}^2} (r-r_o)^2 + \tilde{\mathscr{A}}(r,s) \tag{20}$$

Let $\tilde{\mathscr{A}}(r,s)$ be: $\tilde{\mathscr{A}}(r,s) = \frac{\tilde{B}.r_o}{m} A(\rho,\Theta)$ (21)

with:

$$\begin{cases} \rho = \dfrac{r-r_o}{\epsilon} & \epsilon > 0 \\ \Theta = -ms \end{cases} \tag{22}$$

It is assumed that $A(\rho,\Theta)$ is an even function of Θ with a period 2π. $A(\rho,\Theta)$ also satisfies the normalisation conditions:

$$\begin{cases} A(1,0) = 2 & \dfrac{\partial A}{\partial \rho}(0,\pi) = 0 \\ A(0,\pi) = 0 \end{cases} \tag{23}$$

If the supplementary condition ($\rho = 1$ for $\Theta = 0$ and $\mathscr{A} = 0$) is imposed, a definition of ϵ is obtained:

$$\epsilon^2 = -4\frac{R}{m}\frac{\tilde{B}}{B_z}\frac{{q_o}^2}{q'} \qquad \text{with: } \frac{\tilde{B}}{q'} < 0 \tag{24}$$

and Eq. (20) becomes: $2\rho^2 - A(\rho,\Theta) = -A_o$ (25)

with: $A_o = \dfrac{m.\mathscr{A}}{\tilde{B} r_o}$ (26)

The singular points of Eq. (25) are defined by:

$$\begin{cases} 4\rho - \dfrac{\partial A}{\partial \rho}(\rho,\Theta) = 0 \\ \dfrac{\partial A}{\partial \Theta}(\rho,\Theta) = 0 \end{cases} \tag{27}$$

As $A(\rho,\Theta)$ is an even function of Θ, satisfying conditions (23), the point $\rho = 0$, $\Theta = \pi$ is always singular. For $\Theta = \pi$, we can distinguish two cases according to the relative magnitude of 1 and $\frac{1}{4}\frac{\partial^2 A}{\partial \rho^2}(0,\pi)$, as shown in Fig. 2.

(i) Case Ⓐ

If $\frac{1}{4}\frac{\partial^2 A}{\partial \rho^2}(0,\pi) < 1$, only one singular point exists for $\Theta = \pi$ at $\rho = 0$, and it can be shown that this point is nodal. This situation occurs when q' is not too small. Then, Eq. (25) represents continuous periodic curves for $A_o < 0$, the separatrix for $A_o = 0$ and islands which turn in the same direction for $0 < A_o \leq A(0,0)$, as shown in Fig.3 in the r, Θ coordinate system. ϵ represents the half width of the separatrix.

(ii) Case Ⓑ

If $\frac{1}{4}\frac{\partial^2 A}{\partial \rho^2}(0,\pi) > 1$, Fig. 2 indicates that there are

$$\left[\text{Generally, } \mathscr{P}_v = \eta J^2 + \mathscr{P}_{e(\text{add.heat.})} - \mathscr{P}_{\text{rad.}} - \frac{n(T_e - T_i)}{\tau_{eq.}}\right]^*$$

Assuming that the islands are thin $(\frac{m\epsilon}{r_o} \ll 1)$, Eq. (29) gives:

$$\frac{dT_e}{dA_o} = \frac{\epsilon^2 \mathscr{P}_v}{4\chi_{\perp e}} + \frac{\epsilon^2}{4\chi_{\perp e}} \frac{d\mathscr{P}_v}{dT_e} (T_e(A_o) - T_e(A_{oc})) \qquad (30)$$

If $\delta T_e = T_e(A_o) - T_e(A_{oc})$ is small compared to $T_e(A_{oc}) = T_o$, (where A_o and A_{oc} $(A_{oc} < A_o)$ define a magnetic surface inside the island and its last undestroyed surface, respectively), Eq. (30) can be integrated to give:

$$\delta T_e = \frac{\epsilon^2 \mathscr{P}_v}{4\chi_{\perp e}} (A_o - A_{oc}) \qquad (31)$$

provided that: $\frac{d\mathscr{P}_v}{dT_e} \delta T_e < \frac{\mathscr{P}_v}{2}$.

Assuming that the current density (Eq. (2)) depends on the temperature through the resistivity: $\frac{\delta J_h}{J_{ho}} = \frac{3}{2} \frac{\delta T_e}{T_o}$, it can be shown by using Eq. (31) that:

$$\delta J_h = \left(\frac{3}{8} \frac{J_{ho}}{T_o} \frac{\mathscr{P}_v r_o^2}{\chi_{\perp e}}\right) \frac{\epsilon^2}{r_o^2} (A_o - A_{oc}) \qquad (32)$$

δJ_h represents the difference between the current densities circulating inside and outside the island.

2.5 Field produced by the island - internal solution.

If $\mathscr{A}(r,s)$ is expressed as $\mathscr{A}(r,s) = \mathscr{A}_o(r) + \tilde{\mathscr{A}}(r,s)$, the combination of Eqs. (4) and (7), in the case where $\frac{d\mathbf{P}}{d\mathscr{A}}$ can be neglected, leads to the following equation satisfied by $\tilde{\mathscr{A}}(r,s)$:

$$\Delta_h \tilde{\mathscr{A}}(r,s) = \left(\frac{8\pi p}{p^2 + r^2}\right) \frac{J_{ho}}{B_{ho}} \tilde{\mathscr{A}}(r,s) - 4\pi\, \delta J_h(\tilde{\mathscr{A}}(r,s)) \qquad (33)$$

From the expressions for δJ_h (Eq. (32)) and A_o (Eq. (25)) and taking into account Eqs. (21), (22) and (24), we obtain:

$$4\pi\, \delta J_h(\tilde{\mathscr{A}}(r,s)) = \left(\frac{3\pi}{2} \frac{J_{ho}}{T_o} \frac{\mathscr{P}_v r_o^2}{\chi_{\perp e}}\right) \frac{\epsilon^2}{r_o^2} (A(\rho,\Theta) - A_{oc}) \qquad (34)$$

*Other terms such as the electron cooling resulting from ionisation may need to be taken into account.

Combination of Eqs. (40) and (37) gives:

$$\sum_{n=0}^{\infty} a_n K_n \cos n\Theta = \begin{cases} -N\frac{\epsilon}{r_o}\sqrt{2}\,(a(\Theta)-a(\Theta_o))^{3/2} & -\Theta_o \leqslant \Theta \leqslant \Theta_o \\ 0 & -\pi \leqslant \Theta \leqslant -\Theta_o \text{ and } \pi \geqslant \Theta \geqslant \Theta_o \end{cases} \tag{41}$$

with the normalisation conditions $A(1,0) = 2$, $A(0,\pi) = 0$, $A(\alpha,0) = 2\alpha^2 + A_{oc}$ and $A(0,\Theta_o) = A_{oc}$.

Eq. (41) defines the thermal islands at equilibrium, ϵ being the half width of the separatrix, which is real, if the islands are not destroyed, and imaginary, if the islands are partly destroyed and surrounded by an ergodic zone.

Eq. (41) is equivalent to a non-linear eigen function equation, whose solution has been computed for different values of Θ_o (by taking $K_n = -2mn\frac{\sqrt{p^2+r_o^2}}{p}$ for $n > 1$ (Eq. (19))).

If $\Theta_o = \pi$, the first harmonic dominates and it can be shown that:

$$\frac{\epsilon}{r_o} = -\frac{K_1}{2N} \quad \text{if} \quad |K_1| \lesssim 2m\,\frac{\sqrt{p^2+r_o^2}}{p} \tag{42}$$

When m is not too small, Eq. (42) becomes:

$$\frac{\epsilon}{r_o} = \frac{m}{N}\,\frac{\sqrt{p^2+r_o^2}}{p} \tag{43}$$

(Note that $\epsilon > 0$ (see Eq. (22))).

If $\Theta_o \neq \pi$, the harmonics $n > 1$ play a major role and must be considered in the calculation. However, the result is not sensitive to the precise value of K_1 which has been equated with

$$-2m\,\frac{\sqrt{p^2+r_o^2}}{p}\ .$$

Table I shows that ϵ increases sharply with a slight decrease of α.

Table I

Θ_o	π	$\frac{\pi}{2}$	$\frac{\pi}{4}$	$\frac{\pi}{8}$	$\frac{\pi}{16}$
α	1	0.88	0.77	0.66	0.61
$\frac{r_o}{N\epsilon}$	0.98	0.58	0.26	0.1	0.05

When the surface q = 2 is in the domain where $\mathcal{P}_v$ is negative, large thermal islands (m = 2) may grow and bridge the q = 1 and q = 2 regions, resulting in ergodisation throughout the plasma (disruption). The condition for a disruption to occur can be written: $\mathcal{P}_v < 0$ at q = 2. From the definition of $\mathcal{P}_v$ in the ohmic case (Section 2.4) and using that $\mathcal{P}_{rad} + n(T_e - T_i)/\tau_{eq.}$ is proportional to n^2, it can be deduced that the critical electron density for disruptions increases linearly with the current density, as long as other plasma parameters are maintained constant.

If $\mathcal{P}_v$ is negative for $q \gtrsim 2$, smaller islands (m = 3 to 10) can grow and their interaction creates a large ergodic zone where the confinement is poor. These islands could be the Mirnov modes [8, 9].

(2) When $q' < 0$ and $\mathcal{P}_v > 0$ (which corresponds to an overheating of the plasma), thermal islands may also grow. This case is also described in Fig. 5(a). This could occur in the radial region inside the maximum of a hollow current profile (created by a skin effect or by a peaked Z profile). The growth of this instability leads to mini-disruptions by ergodisation of a large part of the plasma.

(b) $N < 0$:

When N is negative (i.e. $\mathcal{P}_v/q'$ is positive), K_1 is positive, since $K_1/N < 0$. There are no thermal instabilities, but the plasma is unstable with respect to tearing modes. Fig. 5(b) shows the corresponding equilibria curve. In the region where q' is positive, $\mathcal{P}_v$ is positive and the tearing mode is limited by overheating. Correspondingly, in the region where q' is negative, $\mathcal{P}_v$ is negative and the tearing mode is limited by underheating.

(ii) Weak shear case (q' small; case (B) in Section 2.3)

Whatever the sign of q', thermal islands above a critical size (calculated from Eq. (27)) grow independent of the sign of $\mathcal{P}_v$ (corresponding to an underheating (if $\mathcal{P}_v < 0$) or an overheating (if $\mathcal{P}_v > 0$) of the plasma). For example, this situation could occur near the plasma centre in a normal tokomak discharge or near the maximum of a hollow current profile. Moreover, in these cases, the plasma could already be strongly unstable to tearing modes if the q value near the current maximum permits small m number modes to develop. The previous limitation on tearing modes by thermal effects disappears.

4. CONCLUSION

We have shown that thermal islands can grow, when $\mathcal{P}_v/q'$ is negative, $\mathcal{P}_v$ being the net power input to the electrons in the island excluding the conduction term. The size of these islands is limited by ergodisation due to their mutual interaction. In a tokomak, ergodisation leads to disruption for small m numbers (m = 2 at q = 2) or to poor confinement in the outer plasma region, where the power losses are large compared to the input power (underheating). The region located between the q = 1 and $q \simeq 2$ surfaces is generally free from these

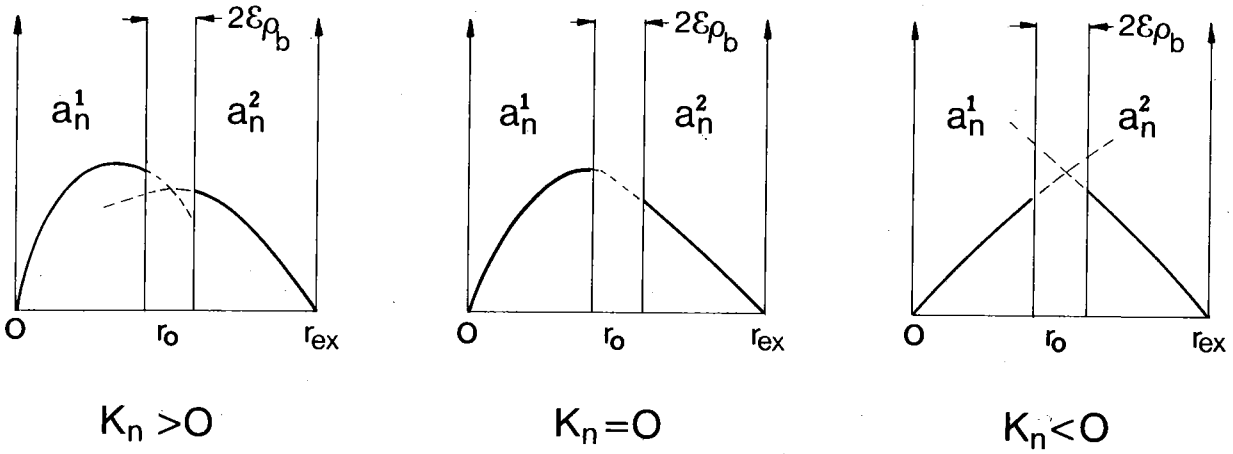

Fig. 1: Solutions of Eq. (16) with the boundary conditions (17) giving a_n (r) versus r for the three cases: $K_n > 0$; $K_n = 0$; $K_n < 0$. (The value of K_n is related to the difference between the $a_n(r)$ gradients each side of r_o).

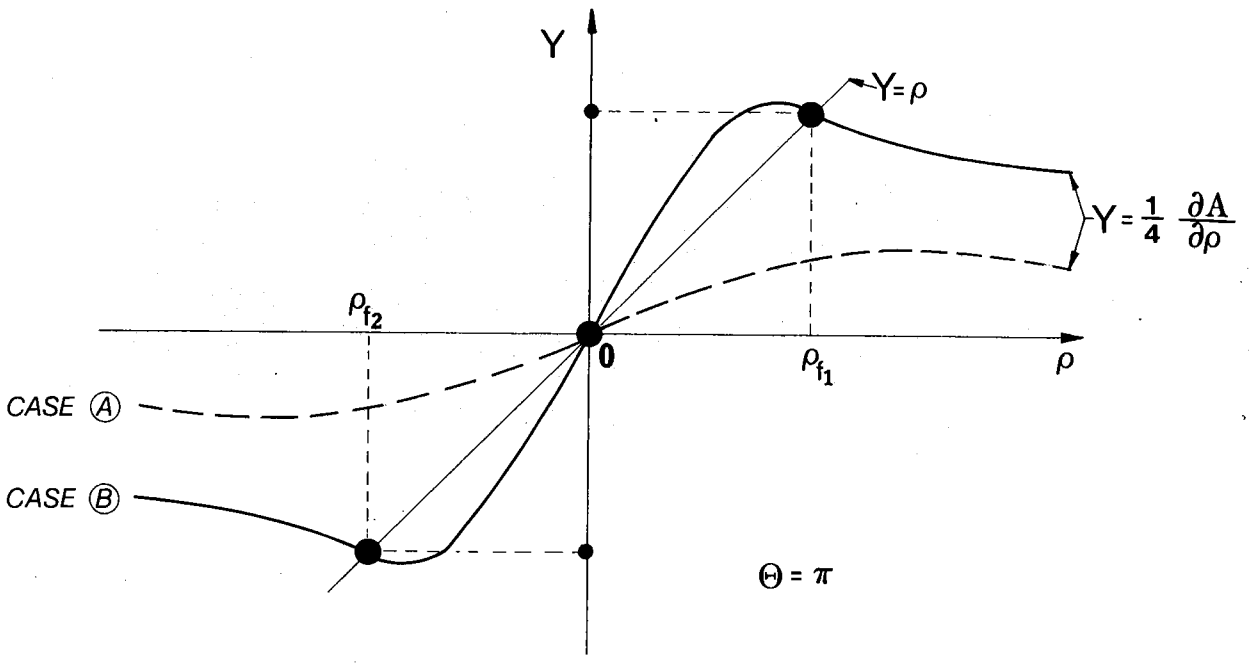

Fig. 2: Singular points of Eq. (25) at $\Theta = \pi$: Case Ⓐ $\frac{1}{4}\frac{\partial^2 A}{\partial \rho^2}(0,\pi) < 1$; and Case Ⓑ $\frac{1}{4}\frac{\partial^2 A}{\partial \rho^2}(0,\pi) > 1$.

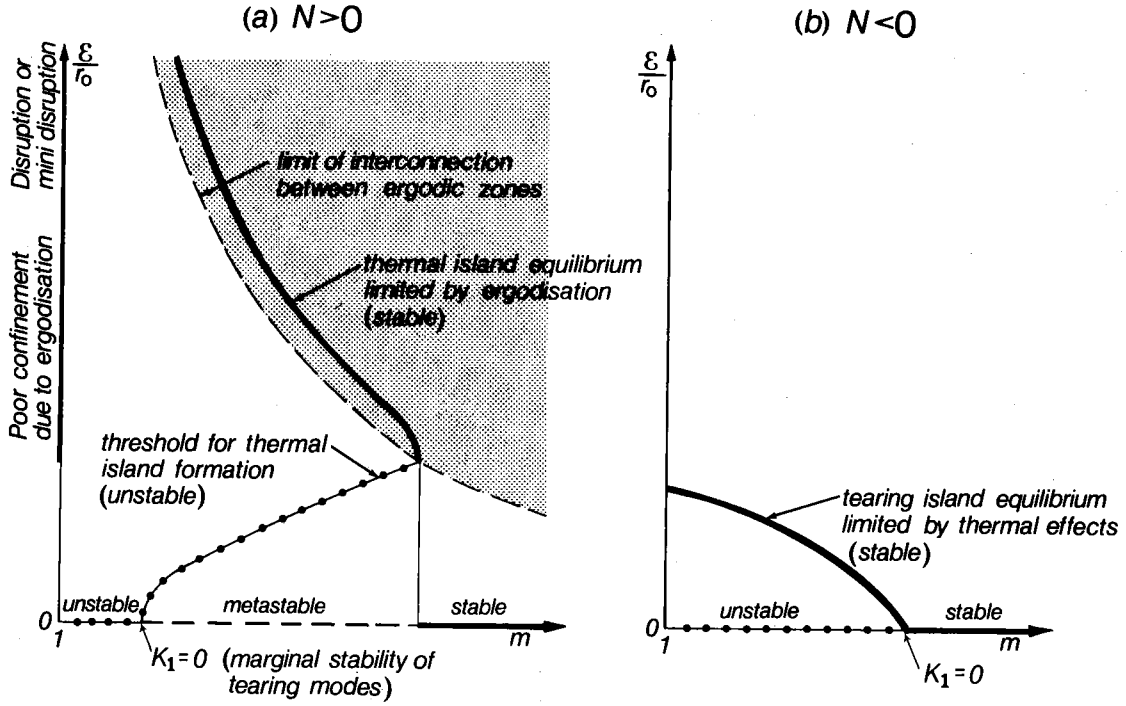

Fig. 5: Equilibria diagrams for the islands for (a) $N > 0$ and (b) $N < 0$. In (a), the shaded area corresponds to a state dominated by ergodic behaviour of magnetic field lines with $\Delta < \epsilon_1 + \epsilon_2$ (see Fig. 4); the clear area corresponds to the case where the magnetic field lines show mainly laminar behaviour with $\Delta > \epsilon_1 + \epsilon_2$ (see Fig. 4).

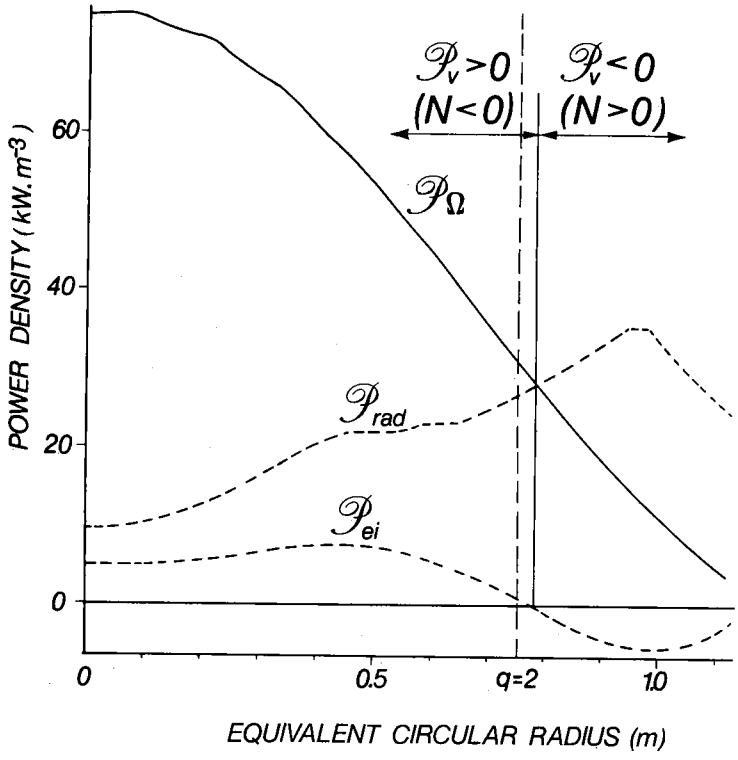

Fig. 6: Radial profiles on JET for ohmic input power density, $\mathscr{P}_\Omega$; radiated power density, $\mathscr{P}_{rad}$; and electron-ion transfer, $\mathscr{P}_{ei}$. The vertical dotted line indicates the position of the q = 2 surface. The vertical full line corresponds to $\mathscr{P}_V = 0$.